Biophysical Journal Volume 70 January 1996 418–429

Directional Loading of the Kinesin Motor Molecule as it Buckles a Microtubule

Frederick Gittes,*‡ Edgar Meyhöfer,* Sung Baek,* and Jonathon Howard*
*Department of Physiology and Biophysics, and ‡Center for Bioengineering, University of Washington, Seattle, Washington 98195-7290 USA

ABSTRACT Single kinesin motor molecules were observed to buckle the microtubules along which they moved in a modified in vitro gliding assay. In this assay a central portion of the microtubule was clamped to the glass substrate via biotin-streptavidin bonds, while the plus end of the microtubule was free to interact with motors adsorbed at low density to the substrate. A statistical analysis of the length of microtubules buckled by single motors showed a decreasing probability of buckling for loads greater than 4–6 pN parallel to the filament. This is consistent with kinesin stalling forces found in other experiments. A detailed analysis of some buckling events allowed us to estimate both the magnitude and direction of the loading force as it developed a perpendicular component tending to pull the motor away from the microtubule. We also estimated the motor speed as a function of this changing vector force. The kinesin motors consistently reached unexpectedly high speeds as the force became nonparallel to the direction of motor movement. Our results suggest that a perpendicular component of load does not hinder the kinesin motor, but on the contrary causes the motor to move faster against a given parallel load. Because the perpendicular force component speeds up the motor but does no net work, perpendicular force acts as a mechanical catalyst for the reaction. A simple explanation is that there is a spatial motion of the kinesin molecule during its cycle that is rate-limiting under load; mechanical catalysis results if this motion is oriented away from the surface of the microtubule.

INTRODUCTION

Kinesin is a motor protein that derives its energy from ATP hydrolysis. It is thought to be responsible for the transport of various types of cargo along microtubules within eukaryotic cells (Brady, 1985; Vale et al., 1985). Kinesin differs from myosin and dynein in that a single kinesin molecule is sufficient to move a microtubule across a glass surface (Howard et al., 1989; Block et al., 1990). This ability suggests that in its chemical cycle, kinesin, unlike myosin for example, spends very little time detached from the filament.

The motor activity of kinesin depends on the longitudinal load, i.e., the force parallel to the microtubule. Hunt et al. (1994) described an assay in which high viscosity slowed microtubule gliding. Svoboda and Block (1994) observed the transport of beads against the restoring force of an optical trap. Meyhöfer and Howard (1995) observed the deflection of a fine glass needle attached to a gliding microtubule. All of these experiments found that kinesin motion along a microtubule slows from an unloaded speed of about 0.5–1.0 μm/s down to stalling at a longitudinal opposing force of about 4–6 pN. An unanswered and physiologically significant question is how motor function depends on the microscopic direction of loading. For example, when a motor transports a large object such as a vesicle along a microtubule (or a bead, in an optical trap experiment) the loading force is not in a line with the motor; considering moment balance, one expects a perpendicular component of force pulling the motor away from the filament.

In the present experiment, we impose on single kinesin motors loads with components both perpendicular and parallel to the motor movement. This is achieved by arranging for buckling of the microtubules along which the motors move. We can then infer the magnitude and direction of the loading forces from the observed bending shapes of the microtubules. Only one parameter, the flexural rigidity EI, is needed to connect bent shapes with the forces that cause the bending (Appendix A), and we have previously determined EI by observing thermal shape fluctuations of microtubules (Gittes et al., 1993). There have been previous discussions relating observed filament bending to force production (Brokaw, 1975; Allen et al., 1985; Amos and Amos, 1991; Bourdieu et al., 1995). Here, we arrange for controlled and repeatable buckling events of a particular type. As shown in Fig. 1, *a* and *b*, we bind a short segment of each microtubule to the glass surface via biotin-streptavidin bonds, linking biotin groups on the microtubule to streptavidin that is indirectly attached to the surface. The major part of the microtubule has no biotin label and does not bind to the surface, but sweeps back and forth in thermal motion. When the free portion with the proper polarity encounters a kinesin molecule the kinesin generates force and buckles the microtubule (if the microtubule is long

Received for publication 12 June 1995 and in final form 13 September 1995.

Address reprint requests to Dr. Jonathon Howard at Department of Physiology and Biophysics, Health Sciences Building, Room G-424, University of Washington, Box 357290, Seattle, WA 98195-7290. Tel.: 206-685-3199; Fax: 206-685-0619; E-mail: johoward@u.washington.edu and gittes@u.washington.edu.

Dr. Meyhöfer's current address is Klinische Physiologie, OE 4210, Medizinische Hochschule Hannover, 30623 Hannover, Germany.

0006-3495/96/01/418/12 $2.00

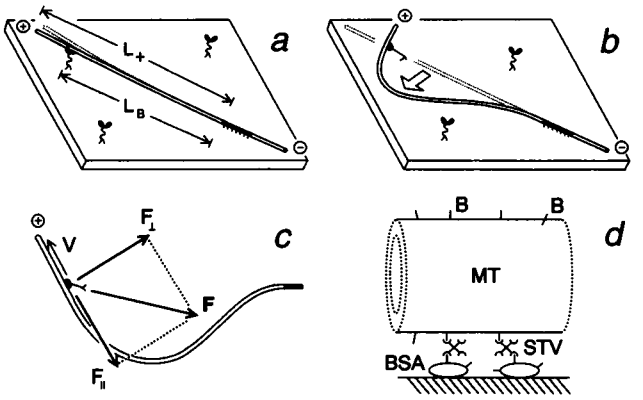

FIGURE 1 Arrangement of the microtubule buckling experiment. Kinesin motor dimensions and microtubule thickness are greatly exaggerated. (*a*) The microtubule is chemically attached ("clamped") to a glass surface along a biotinylated seed segment (*black*). The longer plus end segment (of length L_+; labeled +) fluctuates in thermal motion (*dotted line*) and encounters a kinesin motor on the surface. As the motor tries to move toward the microtubule plus end, a loading force $\boldsymbol{F}$ develops. In *b* the microtubule buckles sideways if the buckling length L_B between the motor and the clamp is large enough. In *c* the situation is viewed from above (in the plane of the surface.) The load $\boldsymbol{F}$ on the motor has a component $F_\parallel$ parallel to the microtubule and a component $F_\perp$ perpendicular to it. Although $F_\perp = 0$ at the onset of buckling, eventually (as shown here) the microtubule swings about the motor position so that $F_\perp$ grows while $F_\parallel$ decreases. $\boldsymbol{F}$ itself also rotates slightly out of alignment with the clamp. (*d*) Attachment of a microtubule to the substrate via biotin-streptavidin bonds, roughly to scale (BSA, bovine serum albumin; STV, streptavidin; B, biotin; MT, microtubule). The microtubule thickness is about 25 nm.

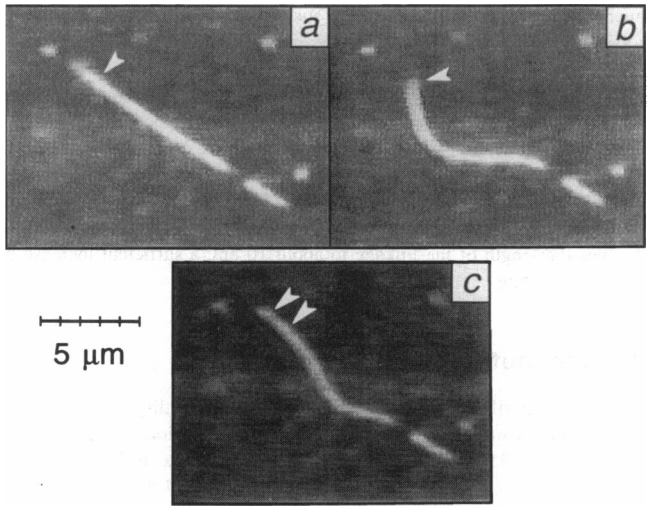

FIGURE 2 Experimental realization of Fig. 1, viewed under fluorescence microscopy. (*a*) A microtubule is "clamped" to a glass surface along the short dark segment toward the lower right, and in *b* is buckled by a kinesin motor on the surface, whose location is indicated by a white arrow. The plus end (longer) and the minus end (shorter) of the microtubule are rhodamine-labeled (see Materials and Methods) and fluoresce brightly. These images correspond to the diagrams in Fig. 1, *a*, *b*, and *c*. The total duration of this event is about 2 s. In *c* a different event, out of line with the clamp, was rejected because it involved at least two motors (*white arrows*), both distinct from the motor in *b*.

enough). Fig. 2, *a* and *b*, shows fluorescence video images of an actual buckling event corresponding to Fig. 1, *a* and *b*. If the event progresses far enough that the microtubule is drastically bent, the component of motor force perpendicular to the microtubule grows large, eventually becoming equal to or greater than the parallel component of force (see Fig. 1 *c*). This rotation of the loading force relative to the microtubule provides an opportunity to compare the relative effects of parallel and perpendicular force components.

Longer microtubules are more easily bent than short ones; a statistical analysis of many buckling events shows consistency with values of parallel stalling force that have been found by the groups mentioned above, although here a precise value is not precisely measured. This consistency serves as a check on our flexural rigidity, *EI*. In cases where the loading force rotates away from the microtubule, we find that the development of a perpendicular force (pulling the motor away from the microtubule) does not hinder the motor as one might have supposed. On the contrary, we consistently find that as the perpendicular component of force rises, the motor speed rises to 1 μm/s or more before the parallel force has greatly declined. Such speeds would be considered fast even in unloaded gliding assays, where motor speeds are typically in the range of 0.5–1.0 μm/s (Hunt et al., 1994). We find that the kinesin motor appears to be catalyzed by a perpendicular loading force, reaching speeds well above those expected for the same parallel load. The effect requires an interpretation in terms of the conformational movement within each mechanochemical cycle of the motor.

MATERIALS AND METHODS

Hybrid microtubules and linkage to the substrate

To arrange buckling events as in Figs. 1 and 2, we bind a short segment of each microtubule to the glass surface via biotin-streptavidin bonds. The bound region of the microtubule is a biotin-labeled seed segment, onto which nonbiotinylated segments have been grown. Nonbiotinylated segments are rhodamine-labeled so that under fluorescence microscopy the seed region is visible as a dark portion along the fluorescent microtubule. The faster-growing end is called the plus end; this fluorescent segment is usually longer than the other (Howard and Hyman, 1993). The longer plus-end segment can undergo buckling because the plus-end-directed kinesin motor is able to exert a compressive force on it.

Microtubules were polymerized from subunits of tubulin and purified by repolymerization followed by phosphocellulose chromatography (Weingarten et al., 1974). Tubulin was cycled again to remove inactive protein. Rhodamine tubulin was made according to the method of Hyman et al. (1991). For biotin-labeled seed regions, cycled tubulin (5 μM) was polymerized with 0.5 mM GMP-CPP for 90 min at 37°C in MES buffer (100 mM MES, 1 mM EGTA, 1 mM $MgCl_2$, pH 6.9), and microtubules were biotinylated with 100 μM biotin-XX (Molecular Probes), quenched with 2 mM potassium glutamate, and airfuged twice to remove excess biotin. Fluorescent, nonbiotinylated segments of the microtubules were grown, also in MES buffer, by adding 5 μl of the biotinylated seeds to a mixture of 10 μM unlabeled and 5 μM rhodamine-labeled tubulin, 4 mM $MgCl_2$, 1 mM GTP, and incubating at 37°C for 20 min. The microtubules were stabilized by diluting 1:20 into BRB80 (80 mM PIPES, 1 mM $MgCl_2$, 1 mM EGTA, pH 6.8) with taxol (10 μM).

The hybrid microtubules were bound along their seed portions to a glass surface. Steric constraints hindered the direct binding of biotin on the

microtubules to streptavidin on the surface; however, this problem was solved by using an indirect linkage, also described by Meyhöfer and Howard (1995) and shown in Fig. 1 *d*. This linkage takes advantage of the multiple (four) binding sites for biotin on each streptavidin molecule. The surface was coated with biotinylated bovine serum albumin (BSA), followed by streptavidin (STV), which bound via some of its sites to the BSA. Microtubules were introduced, and their biotinylated seed regions were bound to unoccupied biotin sites on the STV molecules. Dimensions are shown approximately to scale in Fig. 1 *d*. The BSA intermediate roughly doubles the length of the linkage to about 10 nm, a sufficient increase to facilitate binding.

Kinesin motors

Kinesin was purified from bovine brain by affinity binding to endogenous microtubules using AMP-PNP followed by gel and cation chromatography (Wagner et al., 1991), and was adsorbed onto the glass surface. Adsorbed kinesin densities, in an ordinary gliding assay, would be low enough to ensure single-motor motility. Experiments were done at room temperature. We used two kinesin concentrations, diluting 3000× and 10,000× from the stock solution (typically 100–130 μg/ml kinesin; MW 360,000). From the flow-cell dimensions we estimate the surface density of competent kinesin as very roughly ~0.3/μm^2 for 3000× dilution and ~0.1/μm^2 for 10,000× dilution (including crude factors of 1/10 for unfavorable adsorption to the coverslip (the observed surface), compared to the slide (Howard et al., 1993; Hunt et al., 1994), and 1/2 for incorrect orientation of adsorbed kinesin).

Microtubule bending stiffness

The flexural rigidity of rhodamine-labeled microtubules, grown in PIPES buffer with dimethyl sulfoxide to assist nucleation, was $EI = 2.1 \times 10^{-23}$ Nm^2 (±4.7%), as measured by observing thermal fluctuations (Gittes et al., 1993). However, the present experiments used microtubules grown from rhodamine-labeled tubulin in MES buffer, from seeds polymerized using GMP-CPP, a nonhydrolizable GTP analog.

We corrected the flexural rigidity EI measured by Gittes et al. (1993) for differences in protofilament number P between PIPES-synthesized and MES-synthesized microtubules (polymerization buffer, not the method of nucleation, is the most important determinant of P, because protofilament number can change as the microtubule grows; Chrétien et al., 1992). Microtubules of different P values should have a flexural rigidity EI closely proportional to P^3 (Gittes et al., 1993). Ray et al. (1993) give explicit distributions of P in PIPES ($\bar{P} = 14.03$) and MES ($\bar{P} = 13.52$) (their table 1 contains a rounding error in row 8, where "2%" reflects 1/68 = 1.47%). From this table one finds $EI_{MES}/EI_{Pipes} = (P^3)_{MES}/(P^3)_{Pipes} = 0.90$ (±2.8%), where the uncertainty derives from the statistics of the P distributions. The implied mean stiffness of MES-grown microtubules is $EI_{MES} = 1.9 \times 10^{-23}$ Nm^2 (±5.5%). This value of EI was used in all subsequent inferences of bending force (see Results).

Screening of buckling events

Twenty-seven hours of video recordings were made at kinesin dilutions of 3000× (six preparations) and 10,000× (eight preparations). Each preparation was scanned systematically for a variable length of time, stopping to record when a repeating buckling event was found. Of hundreds of buckling microtubules, many could be rejected after close inspection of the videotape, using two criteria: i) Many events were due at their onset to two motors acting at different points of the microtubule; an example is shown in Fig. 2 *c*. (The onset of buckling determines minimum buckling force; see Results). ii) Each event was inspected for looseness of clamping along the biotinylated segment. Screening was repeated in several rounds of inspection, rating, and consolidation via re-taping. All events were rated as to their ambiguity in the evaluation of criteria i) and ii). Markedly crooked microtubules were also given low grades. Finally, the top three grades were accepted. Pivot points of the buckling microtubules (the putative kinesin motor locations) were identified by hand-tracing shapes to find crossing points of the drawn curves. Distances between pivot points and apparent clamp points were found using Measure hardware and software (M. Walsh Electronics, San Dimas, CA), and were numerically corrected for camera field distortion.

Fig. 3 *a* shows distributions of buckling lengths for grades 1, 2, and 3, representing a total of 142 distinct buckling lengths, for dilutions 3000× and 10,000× combined. Fig. 3 *b* shows the distributions of buckling lengths for dilution 3000×, with 88 buckling lengths; Fig. 3 *c* shows the distributions of buckling lengths for dilution 10,000×, with 54 buckling lengths.

Dilution test of single-motor action

If buckling events are due to single kinesin motors, then the rate of events should decline in proportion to the adsorbed kinesin concentration. Two-motor processes should decrease in rate by the square of the dilution. Table 1 gives event rates for the 14 preparations (and a square-root transformation for statistical comparison of different event rates) to yield a 3000×/10000× rate ratio of 3.1 ± 0.7 (or smaller), comparing favorably to linear dilution (10,000/3000 ≅ 3.3), and unfavorably to a quadratic dilution ratio ($10{,}000^2/3000^2 \cong 11.1$). Additional evidence for single-motor action comes from the buckling-length distributions at 3000× (Fig. 3 *b*) and 10,000× (Fig. 3 *c*). The distributions are not distinguishable ($p = 0.36$, χ^2 with $\nu = 15$ degrees of freedom). The mean buckling force is proportional

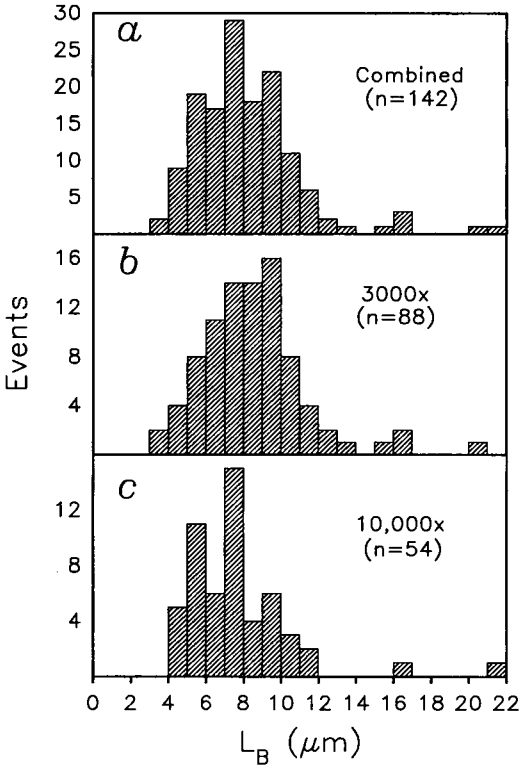

FIGURE 3 Histograms $H(L_B)$ of buckling length L_B (see Fig. 1 *a*), obtained by repeated screening of buckling events drawn from 27 h of videotape comprising 14 preparations (see Table 1). (*a*) 142 distinct buckling lengths at kinesin dilutions (from stock solution) of 3000× and 10,000× (combined). (*b*) 3000× kinesin dilution alone, with 88 distinct buckling lengths. (*c*) 10,000× kinesin dilution alone, with 54 distinct buckling lengths. Some separate events are distinct motors acting on the same microtubule. The shape of the histogram $H(L_B)$ dilutes uniformly with kinesin concentration (see Materials and Methods).

TABLE 1 Observation times t, event numbers N, and square-root rates $\bar{R}^{1/2}$ of buckling events for 14 kinesin preparations diluted from stock solution 3000× and 10,000×*

3000×			10,000×		
Time (h)	N	Rate$^{1/2}$ ($h^{1/2}$)	Time (h)	N	Rate$^{1/2}$ ($h^{1/2}$)
4.49	19	2.06 ± 0.26	3.10	4	1.14 ± 0.35
1.02	10	3.14 ± 0.58	1.20	2	1.29 ± 0.60
1.53	17	3.34 ± 0.46	1.49	10	2.59 ± 0.47
1.56	14	3.00 ± 0.46	1.09	4	1.91 ± 0.59
2.19	28	3.58 ± 0.37	1.35	5	1.93 ± 0.52
1.06	0	0.00 ± 1.32	1.11	1	0.95 ± 0.67
			3.27	22	2.60 ± 0.31
			2.39	6	1.58 ± 0.39

*68% error ranges (in parentheses) reflect Poisson statistics for each observed N; upper and lower error bars were subsequently averaged. Poisson statistics have a large N range (mean ± SD) of $N \cong \bar{N} \pm \bar{N}^{1/2}$, leading to a square-root rate with range $(N/t)^{1/2} \cong \bar{R}^{1/2} \pm (4t)^{-1/2}$, i.e., variation independent of the mean (facilitating comparison of different groups of $\bar{R}$ values; see, e.g., Box et al., 1978). The 10,000× assay is just consistent ($p = 0.066$ with $\nu = 7$). The six 3000× assays are inconsistent ($p = 0.0037$, χ^2 with $\nu = 5$ degrees of freedom) because of two low-rate preparations. If we take the four highest 3000× preparations ($p = 0.8$ with $\nu = 3$) the squared-mean-root (N.B.) rate ratio is still only 3.1 ± 0.7 (or smaller, if no rates are excluded), closer to a linear ratio 10,000/3000 ≅ 3.3 than to a quadratic ratio $(10{,}000/3000)^2 \cong 11.1$. Dilution of events is consistent with single-motor function.

to $1/L_B^2$ (see Results) and so is sensitive to the low-L_B cutoff, yet does not differ significantly ($p = 0.07$) between the 3000× dilution (7.14 ± 0.58 pN) and the 10,000× dilution (8.43 ± 0.63 pN). Thus we find no effect of kinesin dilution on the distribution of buckling lengths found, consistent with the action of single motors.

Shape analysis of buckling images

Extended and uninterrupted buckling such as that in Fig. 2 occurred in relatively few events. Thirty separate motor/filament events were chosen for their visual clarity (in some separate events the same microtubule was being buckled, but by distinct motors at different locations on the surface). These video images (30 frames/s) were digitized frame by frame after enlargement by 4× to allow a finer pixel grid, using hardware and software described above. Variably spaced set of points (10 to 15 points per frame) were distortion-corrected by best-fit linear transformation to a four-point calibration square at the same field location. Points were interpolated to make 100 equally spaced points, so that shape analysis is length-weighted. Fig. 5 *a* shows interpolated points for the entire buckling event of Fig. 2. Eqs. 7 through 9 of Appendix A contain parameters k, ϕ_0, φ_f, and β, which determine shape and orientation of a buckling filament, plus two coordinates to fix its location. A fit of all six parameters to Fig. 5 *a* would fail because of measurement error. Thus we assume that the motor linkage to the surface supports no torque ($\theta'(s) = 0$ at the pivot; see Appendix A), because of the rotational freedom of the kinesin motor (Hunt and Howard, 1993). Also, the coordinates of the pivot point are estimated precisely as the best-fit crossing point of the digitized curves, so that three fitting parameters remain. Assuming nothing about the quality of the clamp, we use coordinates of an effective clamp position as two theoretical parameters; the final parameter is the elliptic modulus k (see Appendix A). We extend the theoretical curve as a straight line beyond the pivot point to compare with the swinging tail of the filament. We minimize the summed squares of closest distances from each data point (x_p, y_p) to the theoretical curve $(x(\phi_p), y(\phi_p))$ described by Eqs. 7 through 9; each closest approach $(x(\phi_p), y(\phi_p))$ was located by a Newton-Raphson algorithm. Overall three-parameter minimization was mainly performed using a downhill simplex method (Press et al., 1992). Parameter starting values were estimated from fits to the linearized Eq. 6 of Appendix A. Each dotted curve of Fig. 5 *b* is displaced sequentially, with the fitted model (*solid curve*) superimposed.

The fitted theoretical curve gives force values and estimates the length of filament that has passed the pivot point in each video frame. For the latter, we measure theoretical arc length S to the point (x_1,y_1) on the theoretical curve that is closest to a fixed estimate of the experimental (not effective) clamp point; (x_1,y_1) should correspond closely to a fixed point on the actual filament. We estimate instantaneous motor speed with a polynomial fit to motor displacement as in Fig. 6 *b*. To impose zero initial speed and to provide sensitivity to the initial motion, time t is transformed to $u = \exp(-1/t)$ in the polynomial and displacement is transformed by the square root of its difference from the straight-line distance from pivot point to estimated clamp point.

RESULTS

Estimating maximum motor force from buckling lengths

To estimate the maximum force, F_{max}, that a motor can exert parallel to the axis of the microtubule, we observed a great many buckling events like that of Fig. 2 (although the great majority did not reach such a pronounced degree of bending). We then produced a histogram of buckling lengths, L_B, which is the distance between the kinesin motor and the clamp. The Euler stability formula for a rod under a compressive force, with a clamp at one end and zero torque at the other (due to the large rotational compliance of the kinesin molecule; Hunt and Howard, 1993) provides a minimum buckling force, F_B, which must be less than or equal to the maximum motor force, F_{max}:

$$F_{max} \geq F_B \cong 20.19 \times \frac{EI}{L_B^2}. \quad (1)$$

(see Appendix A). We seek a force limit F_{max} of the motors by looking for a cutoff or sharp decrease in the buckling probability $f_0(L_B)$ below some particular L_B.

In Appendix D we deduce the probability per unit length $f_0(L_B)$ that a kinesin motor, a distance L_B from a clamped section of a microtubule, will buckle the microtubule. Because of experimental biases, the observed buckling-length histogram $H(L_B)$ in Fig. 3 *a* is not simply proportional to $f_0(L_B)$; one must divide out two experimental biases that depend on the length L_+ of the plus-end region of the microtubule (see Appendix D).

$f_0(L_B)$, obtained from $H(L_B)$ in Fig. 3 *a*, is shown up to a constant factor in Fig. 4, and represents a probability distribution of putative single-motor buckling events from which experimental biases have been removed. This distribution rises below about 8–10 μm; it also falls at higher L_B, as will be discussed later. Of main interest is the rising portion, which suggests that buckling at lengths shorter than 8–10 μm requires greater forces than the motors can typically develop. Using the flexural rigidity $EI = 1.9 \times 10^{-23}$ Nm^2 in Eq. 1, events with L_B = 8–10 μm should correspond to buckling forces of 4–6 pN. These results are consistent with the maximum kinesin force of 4–6 pN

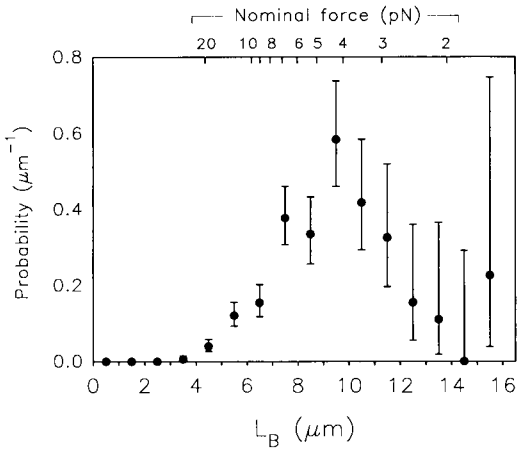

FIGURE 4 Bias-compensated probability of buckling, $f_0(L_B)$, as a function of buckling length L_B. $f_0(L_B)$ is obtained by dividing the histogram in Fig. 3 *a* by an exponential of decay length 2.80 μm (estimated via Fig. 11). The units of $f_0(L_B)$ contain an arbitrary factor. The 68% confidence limits reflect Poisson counting statistics for each bin of Fig. 3 *a*. The nominal force at the top of the figure is the estimated minimum buckling force F_B, parallel to the microtubule, obtained from the Euler stability formula $F_B = 20.19 \times EI/L_B^2$ by assuming a flexural rigidity of $EI = 1.9 \times 10^{-23}$ Nm^2. The buckling probability declines for buckling forces either larger than about 5–6 pN or smaller than about 4 pN. We interpret the decline at low L_B (high force F_B) as consistent with a maximum kinesin motor force of approximately 5 pN, except for some events that may be due to aberrant microtubules. We attribute the decline at large L_B (low force F_B) to the curving of longer microtubules away from the surface.

found by other experiments (Hunt et al., 1994; Svoboda and Block, 1994; Meyhöfer and Howard, 1995).

Dependence of motor speed on nonparallel loads

A mathematical shape analysis was applied to a relatively small number of events that underwent a smooth and extended buckling. Thirty separate motor/filament events were chosen for their visual clarity.

Fig. 5 *a* shows digitized sets of points for the event of Fig. 2, which is perhaps our best buckling event in terms of duration, smoothness of bending, and visual clarity. In Fig. 5 *b*, each curve of Fig. 5 *a* is shown (*dotted curves*), displaced sequentially, with a superposed theoretical model (*solid curves*) that has been fit to the experimental points. An axis is drawn from the origin, running through the estimated pivot point on each theoretical curve.

Fig. 6 *a* shows the tangential and perpendicular components of force at the pivot point as a function of time, obtained from each theoretical curve in Fig. 5 *b* (assuming $EI = 1.9 \times 10^{-23}$ Nm^2; see Materials and Methods). Because of our choice of theoretical parameters, these force estimates are independent of the quality of the clamp and are independent of whether the motor is exactly in line with the clamped region. Fig. 6 *b* shows the arc length S of the filament (in microns) that has passed by the pivot point as a function of time (this arc length represents the displacement of the kinesin motor along the filament); Fig. 6 *b* also shows

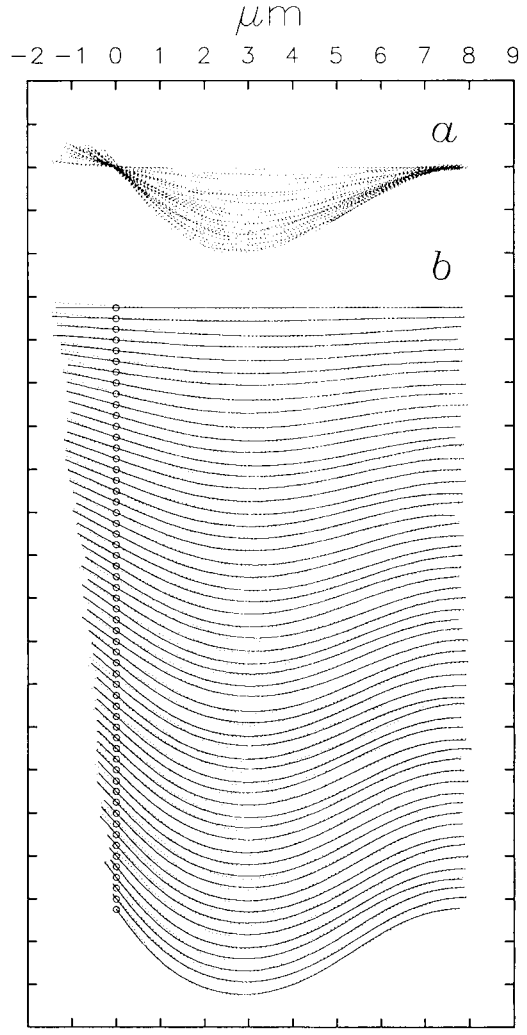

FIGURE 5 (*a*) Digitized curves covering 2.2 s at 30 frames/s, obtained from video frames including Fig. 2, *a* and *b*. Each of the 57 curves was obtained by selecting between 10 and 15 points, correcting for local distortion, and interpolating 100 points to allow a length-weighted analysis. (*b*) The same digitized buckling profiles (*dotted curves*) displaced vertically and fitted to theoretical curves (*solid curves*) as described in Materials and Methods. Given the ~0.5 μm resolution of the video images (compare Fig. 2), the agreement is quite good. A small circle on each curve indicates the estimated pivot point, presumably the location of the kinesin motor.

a displacement curve that has been fitted to the displacement points (see Materials and Methods). The fitted motor speed reaches just over 0.8 μm/s, which is similar to unloaded kinesin gliding speeds.

Combining the time derivative of the fitted displacement curve in Fig. 6 *b* with the estimated force values in Fig. 6 *a*, one obtains force-velocity relations for the components of loading force parallel and perpendicular to the microtubule, shown in Fig. 7 for five different microtubules. Fig. 7 *a* superposes data from two separate events involving the same filament and motor event (that of Fig. 2), showing the overall reproducibility of the analysis from digitization to the final fitting. Fig. 7, *b* through *e*, shows four other events

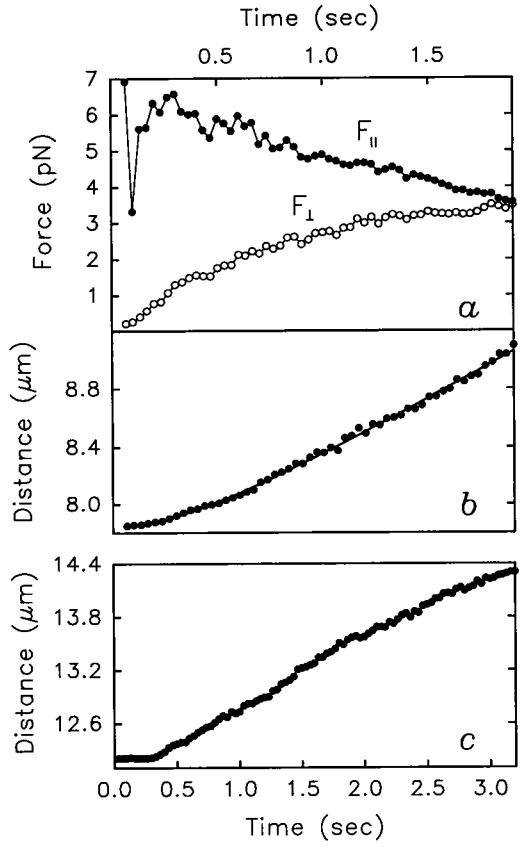

FIGURE 6 Forces and displacements obtained from fitted theoretical curves. (*a*) Components $F_{\parallel}$ and $F_{\perp}$ of loading force on the kinesin motor. $F_{\parallel}$ and $F_{\perp}$ are parallel and perpendicular to the microtubule, respectively (see also Fig. 1 *c* for definitions of $F_{\parallel}$ and $F_{\perp}$) and are obtained from the fitted theoretical curves in Fig. 5 *b* assuming a flexural rigidity of $EI = 1.9 \times 10^{-23}$ Nm^2. (*b*) The total arc length S of filament (in microns) that has passed by the pivot point (the kinesin motor) versus time, obtained from fitted theoretical curves. (*c*) Total arc length S as in *b*, for a separate event with a low load ($F_{\parallel} < 3$ pN) and a long buckling length event ($L_B = 12.2$ μm). The initial velocity is about 0.8 μm/s at the onset of buckling. Here, in contrast to *b*, the motion begins abruptly, ruling out hydrodynamic loading effects (Appendix B).

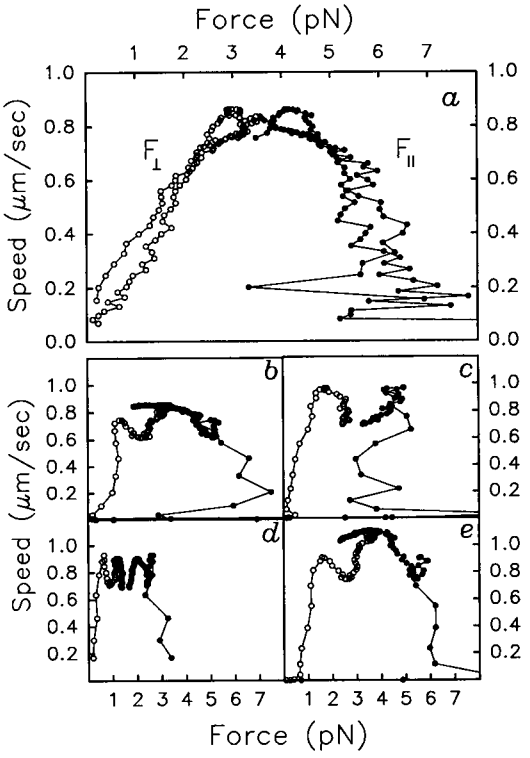

FIGURE 7 Kinesin force versus speed, estimated from microtubule buckling events. (*a*) Force versus speed plots for two events involving the same kinesin motor and microtubule, superimposed, to show overall reproducibility. One event is that of Fig. 6, *a* and *b*. Vertical axis: Motor speed (in μm/s) is computed from a fitted displacement curve as in Fig. 6 *a*. Horizontal axis: Components $F_{\parallel}$ and $F_{\perp}$ of load computed as in Fig. 6 *b*. $F_{\perp}$ (●) and $F_{\perp}$ (○) are parallel and perpendicular to the microtubule, respectively (see also Fig. 1 *c* for definitions). In *b* through *e*, similar force-velocity plots are shown for events involving four other microtubules. A consistent feature of these plots is the attainment of relatively high motor speed while the parallel load is still fairly large.

in which extended and apparently uninterrupted bending takes place.

For many of the buckling events analyzed, the experimental fits were poor because of digitizing noise. However, the attainment of high speeds even under large loads was a consistent finding.

DISCUSSION

We have described results of two complementary analyses of our buckling-microtubule experiment. The first was an estimate of the maximum motor force F_{max} made by a statistical analysis of the buckling forces implied by the Euler stability formula (Eq. 1) applied to many buckling events. The second analysis, applied to fewer events, used a nonlinearized mathematical model of bending to obtain motor speeds and force components both parallel and perpendicular to the microtubule as a function of time.

Maximum motor force

The probability distribution for single-motor buckling events (Fig. 4) decreases as L_B decreases below about 8–10 μm. This is consistent with a motor force limit of roughly 4–6 pN found by Hunt et al. (1994), Svoboda and Block (1994), and Meyhöfer and Howard (1995). The distribution $f_0(L_B)$ still decreases above 10 μm, even after our compensation for bias, which we believe to be due to an inability of motors to reach the filament far from the clamped region; because most in vitro microtubules contain slight bends (Gittes et al., 1993), the seeded segment of a microtubule may tend to attach so that the microtubule bends upward, away from the surface.

The maximum-force analysis suffers from several uncertainties, which probably account for the lack of a sharp cutoff of buckling lengths corresponding to a unique maximum force: 1) The Euler formula (Eq. 1) assumes a well-

clamped rod, and a pivot point (motor position) that is in line with this clamp. In practice, the motor and the clamp may be misaligned by up to ~1 μm. (Note that the misalignment due to the motor acting at the side, rather than the center, of the microtubule is much smaller, only ~15 nm.) Using the theory of Appendix A one can show that motor misalignment or clamp looseness by 5°, corresponding to a misalignment ~1 μm, reduces the maximum parallel loading force to 80% of the Euler value (10° of misalignment gives a reduction to 67%). Ten of 30 shape-analyzed events seemed to exhibit clamp looseness or misalignment that had not been detected by eye, so that Euler forces would be exaggerated by an average of 12%. 2) The microtubules have a distribution of protofilament numbers (Ray et al., 1993) and are therefore expected to have a distribution of stiffnesses (see Materials and Methods). We estimate that the spread in protofilament number found in Ray et al. would broaden the data in Fig. 4 by ±10% in the forces. 3) The clamp looseness and protofilament number variation cannot explain the shortest buckling events, of lengths 4.5 μm, which would require forces of about 19 pN. It is possible that these shortest events correspond to rare, flexible microtubules (e.g., containing 10 or fewer protofilaments) or to rare double-motor events.

Vector force and motor displacement

The force and displacement curves shown in Figs. 6 and 7 are the first estimates of single-motor force generation in the presence of a known perpendicular component of loading force. As the load becomes nonparallel to the microtubule, we infer from Fig. 7 that a growing perpendicular component of force does not hinder the motor as it approaches its maximum speed (about 0.8–1.0 μm/s). Instead, the motor speed increases to high values well before the parallel force drops appreciably. In contrast, Fig. 8 shows data obtained in our laboratory by Hunt et al. (1994) (*open circles*), who measured motor speed versus drag force, using a highly viscous buffer solution, and forces and velocities obtained from the deflection of thin glass needles by individual kinesin motors by Meyhöfer and Howard (1995) (filled circles). These previous results from this laboratory, as well as results obtained by other laboratories (Svoboda and Block, 1994), show a motor speed, plotted versus the parallel component of load, that decreases roughly along a line from a maximum unloaded speed to stalling at a maximum force near 5 pN.

A possible interpretation of the highly nonlinear speed-force curves shown in Fig. 7 is that we have seriously underestimated the flexural rigidity of the buckling microtubules. As a result, the initial forces might be much smaller than we believe and the high initial speeds might simply reflect this low force. However, this interpretation can be ruled out by the shape analysis of the early velocity profiles of the buckling filaments. Near the onset of buckling, when the force is mostly parallel, we often see the motor move slowly, consistent with it being highly loaded. This is clear in Fig. 6 *b*, and it indicates that our estimates of the loading force and the maximum kinesin motor force are reasonable. In contrast, very low-force events at longer buckling length begin abruptly, as for example in Fig. 6 *c*. The latter abruptness also supports our arguments in Appendix B against any artifactual slowing due to hydrodynamic drag.

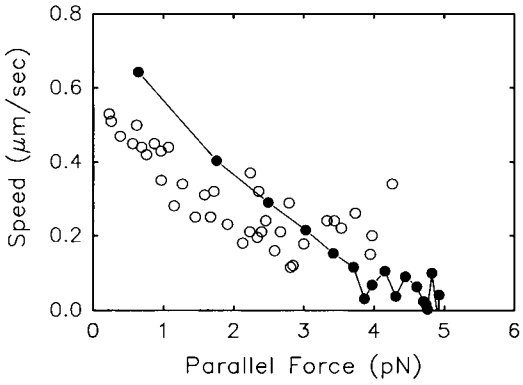

FIGURE 8 Previously obtained plots of kinesin motor speed versus parallel loading force $F = F_{\parallel}$, made in our laboratory. Hunt et al. (1994) (○) deduced viscous forces from observed microtubule gliding speeds in viscous solution; Meyhöfer and Howard (1995) (●) measured motor force by observing the deflection of a glass needle. Neither of these experiments exhibited the combination of relatively high motor speed with large parallel load that is apparent in the plots of motor speed versus force in microtubule-buckling experiments (Fig. 7).

The most direct interpretation of our results is that a perpendicular component of load facilitates the motor function, so that under a perpendicular load the kinesin motor moves faster for a given parallel load.

The vector nature of motor loading

Our results indicate that single kinesin motors move faster, against a given parallel load, when a component of load perpendicular to the filament is present. In the tradition of myosin cross-bridge models (Huxley, 1957; Hill, 1974), later applied to kinesin as well (Leibler and Huse, 1993), motor molecules have been pictured as intrinsically one-dimensional mechanochemical transducers, a viewpoint that may be appropriate for myosin in muscle filaments. But to explain effects specifically caused by a perpendicular load, a purely one-dimensional formalism is inadequate. Furthermore, perpendicular force can only couple to motions of the motor perpendicular to the filament. Because there is no net motion in this direction, it follows that we must consider not just macroscopic motor movement, but changes that are microscopic and internal to the cycle of the motor molecule itself.

We consider the mechanochemical cycle of a kinesin motor domain as it moves along a fixed microtubule (Fig. 9 *a*). This picture is equivalent to our experiment; however, in our experiment it is the microtubule that is moving (Fig. 1 *c*). The loading force $\boldsymbol{F}$ has components $F_{\parallel}$ and $F_{\perp}$. We

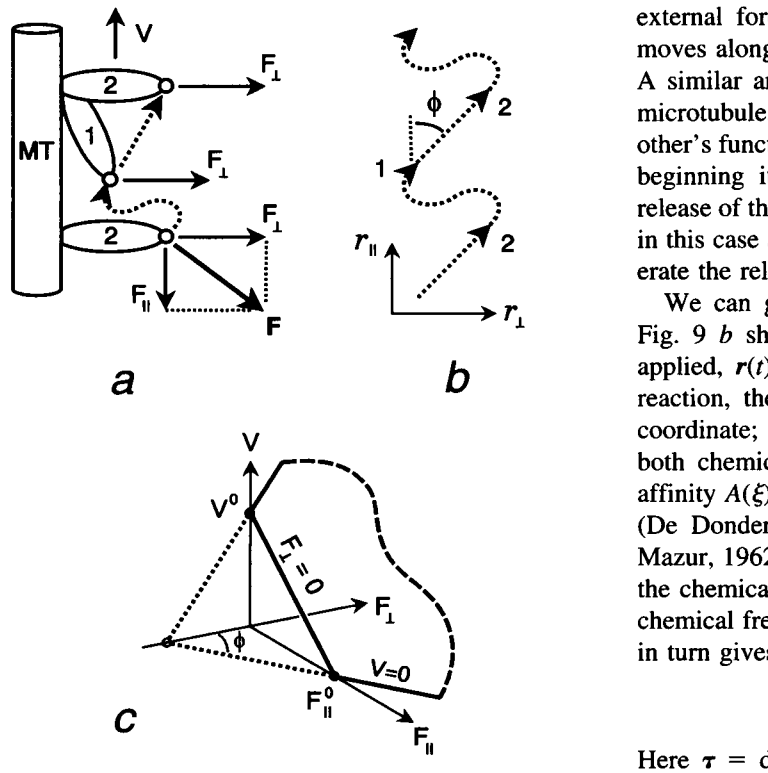

FIGURE 9 (*a*) Idealized situation in which a kinesin motor domain moves along a fixed microtubule under a load that is not parallel to the microtubule. The vector force F and velocity V are oriented as in the buckling experiment (see Fig. 1 *c*); however, in our experiment it is the microtubule and not the motor that is moving. The plane of this figure, like that of Fig. 1 *c*, is the plane of the glass surface; also note that the motor moves along the side of the microtubule both here and in Fig. 1 *c*. The load F has components $F_\perp$ and $F_\parallel$ (parallel and perpendicular to the microtubule). The cycle of the motor includes points, such as 1, where the point of application of F is closer to the microtubule and points, such as 2, where this point is farther away. (*b*) Spatial path $r(t)$ of the mechanochemical kinesin cycle in *a*. The discussion in the text focuses on a hypothetical portion of the cycle, 1→2, that is rate-limiting under load and has some orientation (angle ϕ) relative to the microtubule axis. (*c*) Diagram of a force-velocity plane (see Discussion) obtained by assumption of both a single rate-limiting step in the cycle and of a linear dependence of rate on mechanochemical affinity. The orientation ϕ of the plane $V(F_\parallel,F_\perp)$ is also the orientation angle of the rate-limiting step in the cycle. Motor loading by a parallel force (Fig. 8) is labeled by $F_\perp = 0$; our buckling events (Fig. 7) explore loads with $F_\perp > 0$.

follow the motion of a point r where the loading force acts; r has components $r_\parallel$ and $r_\perp$. Point 1 of the cycle is nearest the microtubule and point 2 is furthest from the microtubule; these are separated in height by $\Delta r_\perp$. A parallel load $F_\parallel < 0$ slows the motor by coupling the change $\Delta r_\parallel$, to an unfavorable energy increase $+F_\parallel \Delta r_\parallel$. Now $F_\perp > 0$ couples 2→1 to an unfavorable energy increase, $+F_\perp \Delta r_\perp$, but it also couples 1→2 to an opposite energy decrease, $-F_\perp \Delta r_\perp$. Because we found that motor speed increases with $F_\perp > 0$, the rate effect on the 1→2 rate must be rate-limiting under load.

The preceding argument does not depend on there being only one head as in Fig. 9 *a*. All that matters is that the external force F acts (does work) on some point r that moves along some spatial path relative to the microtubule. A similar argument could be made if, between r and the microtubule, there are two kinesin heads, affecting each other's function. For example, one head may be hindered in beginning its cycle because it must wait for a delayed release of the other head (see, e.g., Peskin and Oster, 1995); in this case a perpendicular component of force may accelerate the release.

We can generalize by using reaction thermodynamics. Fig. 9 *b* shows the path of the point where the load is applied, $r(t) = (r_\parallel(t), r_\perp(t))$. Because this is a chemical reaction, the distance ξ traced by $r(t)$ is also a reaction coordinate; $r(\xi)$ describes the mechanochemical coupling, both chemical-to-mechanical and vice versa. A chemical affinity $A(\xi) = -\partial G/\partial \xi$ is associated with each value of ξ (De Donder and van Rysselberghe, 1936; de Groot and Mazur, 1962), where $G(T, p, \xi)$ is the Gibbs free energy of the chemical system. Under a load, we define a mechanochemical free energy $\tilde{G}$, with $d\tilde{G} = -A d\xi - F \cdot dr$, which in turn gives a mechanochemical affinity

$$\tilde{A}(\xi) = -\partial \tilde{G}/\partial \xi = A(\xi) + \tau \cdot \mathbf{F}. \qquad (2)$$

Here $\tau = d\mathbf{r}/d\xi$ is a unit vector tangent to the path $\mathbf{r}(t)$. Nonequilibrium thermodynamics assumes that the reaction rate $d\xi/dt$ (here, the rate of conformational change) is some function of the affinity $\tilde{A}(\xi)$ (de Groot and Mazur, 1962). No matter what this specific rate dependence is, Eq. 2 specifies how the external force couples to the system: via a vector τ that points along the direction of the microscopic movement of the motor molecule.

If near one point $\xi = \xi^0$, $\tau(\xi^0) = \tau^0$, the rate is especially sensitive to changes in $\tilde{A}(\xi)$, then under load this becomes the rate-limiting point in the cycle, and Eq. 2 implies that overall velocity will depend on $\tau^0 \cdot \mathbf{F}$, where τ^0 is the direction of the rate-limiting motion. For both a rate-limiting step and a linear dependence of rate on $\tilde{A}(\xi)$ at that point (commonly assumed; de Groot and Mazur, 1962), Eq. 2 predicts a linear relationship between $F_\parallel$ and V, as found by Hunt et al. (1994), Svoboda and Block (1994), and Meyhöfer and Howard (1995). Plotting V versus $F_\parallel$ and $F_\perp$ (and under the assumptions just mentioned) Eq. 2 more generally predicts a force-velocity plane, as shown in Fig. 9 *c*, and described by the relation

$$V(\mathbf{F}) = V^0 + \alpha \cdot \mathbf{F}, \qquad (3)$$

with

$$\alpha = (V^0/\tau_\parallel^0 F_\parallel^0)\tau^0. \qquad (4)$$

The orientation of the plane gives the angle $\phi = \tan^{-1}(\tau_\perp^0/\tau_\parallel^0)$ of rate-limiting conformational change within the motor, as indicated in Fig. 9 *c*.

On a phenomenological basis alone, the force-velocity plane of Fig. 9 *c* explains our data well. If a kinesin motor starts out barely stalled ($F_\parallel = F_\parallel^0$, $F_\perp = 0$) then, as the microtubule buckles, one moves not up a straight line to

$V = V^0$, but to the right, up the $F_\perp > 0$ force-velocity plane. Thus V can increase dramatically while the parallel load $F_\parallel$ is still large. We can in fact calculate the force-velocity diagrams that would result. Bending theory determines the path of $(F_\parallel, F_\perp)$; using the force-velocity plane of Fig. 9 *c* along this path yields the force-velocity relations shown in Fig. 10, for various angles ϕ of the rate-limiting direction τ relative to the microtubule. Fig. 10 *c*, for example, shows a strong qualitative resemblance to Fig. 7 *a*. Kinesin behavior under load can be explained by the presence of a movement within the kinesin cycle that is rate-limiting under load, oriented at a substantial angle (perhaps 45° or more) away from the axis of the microtubule itself.

CONCLUSIONS

Our results indicate that the loading of individual molecular motors is fundamentally a three-dimensional, not a one-dimensional problem. Our buckling experiments, although they lack the precision that has been obtained in longitudinal motor loading experiments, explore the effects of a nonparallel loading force; in fact, they provide a continuous change of loading from wholly longitudinal force to a perpendicular component of force that is even larger than the longitudinal component. We find that a perpendicular component of force, tending to pull the kinesin motor away from the microtubule, appears to facilitate, not hinder, motor function. We have discussed above how this effect is thermodynamically related to the internal conformational changes that take place in the kinesin molecule during its cycle; it particular, it is consistent with a certain movement within the motor cycle that is rate-limiting under load and is directed at a substantial angle away from the filament (schematically, change 1→2 in Fig. 9). In this sense, we have seen how external force may ideally be viewed as a three-dimensional "external field" that can be used to probe the microscopic conformational changes within the motor molecule.

In the preceding discussion, the distinction between chemical reaction path and the path of mechanical motion has disappeared. In this light, it is appropriate to regard the parallel speeding up of a motor by a perpendicular load as an example of mechanical catalysis, because there is no net motion, and thus no net mechanochemical reaction, in the perpendicular direction itself.

We also emphasize that our thermodynamic discussion of loading applies not only to just a single kinesin head, but to the combined action of both kinesin heads.

Our observations argue strongly against the idea that kinesin motors slow under load because they slip back during a detached period, which has been discussed recently (Svoboda and Block, 1994; Meyhöfer and Howard, 1995). Any detached time should increase as the motor is pulled away from the microtubule, so there should be more slippage and the motor should be slower, not faster. Our results seem easily understandable only if the chemical cycle is well coupled to mechanical load, which is why we have discussed theoretical loading behavior in such a context.

Finally, our observations and discussion of motor protein behavior under nonparallel loading are certainly important, not just to in vitro force measurements, but to the physiology of cellular transport. Single motors, or a small number of motors, carry cargoes much larger than themselves through a viscous and obstructive intracellular medium. Thus we expect that the forces on the motors change unpredictably in both magnitude and direction. It would be an appropriate feature of such motor molecules if the loading forces that threaten to pull the motor away from the filament, in fact, enhance its function.

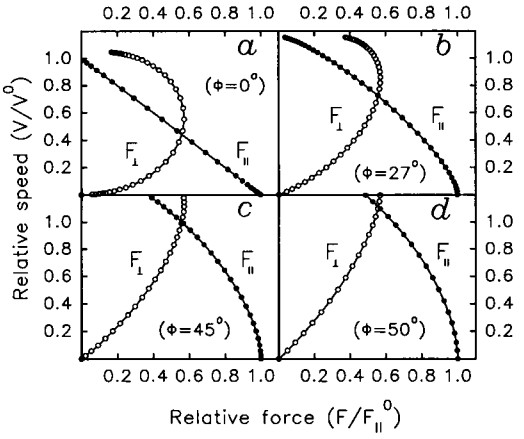

FIGURE 10 Model force-velocity relations predicted by the force-velocity plane of Fig. 9 *c*, when the maximum motor force $F_\parallel^0$ is just equal to the Euler buckling force F_B. Trajectories of the force vector $\boldsymbol{F} = (F_\parallel, F_\perp)$ for these buckling events are projected upwards onto the $V(F_\parallel, F_\perp)$ plane to produce these curves, which should be compared with experimental results in Fig. 7. Symbols are placed at equal time intervals Δt. Both $F_\parallel$ and $F_\perp$ are given relative to $F_\parallel^0$, and speed V is relative to the unloaded gliding speed V^0. Time units are $(EI/F_\parallel^0)^{1/2}/(2V^0)$ (~1 s in our experiments). Plots *a* through *b* assume four different angles $\phi = \tan^{-1}(\tau_\perp^0/\tau_\parallel^0)$, relative to the filament, of a step that is rate-limiting under load (see Fig. 9): (*a*) $\phi = 0°$, $\Delta t = 0.9$; (*b*) $\phi = 27°$, $\Delta t = 0.3$; (*c*) $\phi = 45°$, $\Delta t = 0.18$; (*d*) $\phi = 50°$, $\Delta t = 0.18$. A large angle ϕ in the rate-limiting step (*c* or *d*) would explain the relatively high motor speed at large $F_\parallel$ that is found experimentally (see Fig. 7).

APPENDIX A: THEORETICAL BUCKLING SHAPES AND FORCES

The theory for bending microtubules only depends upon the flexural rigidity EI (see Materials and Methods, and Appendix C). For a microtubule without any "intrinsic" shape (Gittes et al., 1993) the bending free energy per unit length is $g(s) = EI(d\theta/ds)^2/2$, where s is the arc length along the filament and $\theta(s)$ is the tangent angle of the filament. This $g(s)$ is an expansion of the free energy G in the curvature of the filament, and so the bending theory is not dependent upon the microscopic structure of the filament except through the value of the flexural rigidity EI. Derivations of bending equations (originating with Euler) may be found in, e.g., Love (1927) and Landau and Lifshitz (1986). Minimization of the total bending energy leads to an equation

$$\theta''(s) = \beta^2 \sin(\theta(s) - \varphi_f), \qquad (5)$$

where $\beta^4 \equiv (F_\parallel^2 + F_\perp^2)/(EI)^2$ is related to the magnitude of force on the filament, and φ_f is the angle of this force with the parallel axis. To first order in a slight deflection $y(s)$, where $y'(s) = \theta(s)$,

$$y'''(s) + \beta^2 y'(s) = -F_\perp/EI, \tag{6}$$

which is the linearized equation for the buckling of a filament with length $L = L_B$ under longitudinal compression (i.e., in the parallel direction). For a filament clamped at $s = 0$ and hinged at the point $s = L_B$ (i.e., $y(0) = \theta(0) = y'(0) = \theta'(L_B) = y''(L_B) = 0$) with a compressive force $-F_\parallel$ applied at the hinge point, Eq. 6 has a solution $y(s) = \beta(L_B - s) + \sin \beta s - L_B \cos \beta s$, provided that $\tan \beta L_B = \beta L_B \cong 4.493$. This condition gives the Euler formula (Eq. 1) for the minimal buckling force.

Eq. 5 also has exact solutions that can be written in various equivalent ways (Love, 1927; Landau and Lifshitz, 1986). We adopt

$$\beta s = \int_{\phi_0}^{\phi(s)} \frac{d\phi}{\sqrt{1 - k^2 \sin^2 \phi}} \equiv [F(\phi(s), k) - F(\phi_0, k)], \tag{7}$$

$$k \sin \phi(s) = \sin \tfrac{1}{2}(\theta(s) - \varphi_f), \tag{8}$$

where $F(\phi, k)$ is the incomplete elliptic integral of the first kind and k is the elliptic modulus (Gradshteyn and Ryzhik, 1980). Equations 7 and 8 implicitly relate θ and s, and the initial buckling of a straight rod corresponds to $k = 0$ and $\phi_0 \approx -2.923$. The natural parameter of the curve is $\phi(s)$, not the arc length s. Boundary conditions determine k, ϕ_0 $(= \phi(0))$, φ_f, and $\beta = (F/EI)^{1/2}$; φ_f determines the direction and β the magnitude of the force on the motor at the pivot point.

The coordinates x and y along the curve are

$$x(\phi(s)) = \int_0^s \cos \theta(s')\, ds', \quad y(\phi(s)) = \int_0^s \sin \theta(s')\, ds', \tag{9}$$

where the correct k and ϕ_0 must be found to produce an end point $x = X(k,\phi_0)$, $y = Y(k,\phi_0)$. Boundary conditions, such as $Y(k,\phi_0) = 0$, are expressions involving complete and incomplete elliptic integrals. Finally, the proper dimensionless buckling shape must be scaled to the correct L, which determines β and hence the force magnitude. Relative to the filament, the tangent and perpendicular components of force at the pivot point (see Fig. 1 *a*) are

$$F_\parallel = EI\beta^2(1 - 2k^2), \tag{10}$$

$$F_\perp = 2EI\beta^2 k \sqrt{1 - k^2}. \tag{11}$$

APPENDIX B: HYDRODYNAMICS OF FILAMENT BUCKLING

At the usual kinesin motor speeds (~1 μm/s) longitudinal drag on the microtubule should be negligible (~0.05 pN; see Hunt et al., 1994) compared to motor forces. For a buckling filament, however, the initial displacement S of the motor is change in arc length of $y(s)$,

$$S \approx \frac{1}{2} \int_0^L ds (dy/ds)^2. \tag{12}$$

Because S is proportional to the square of the amplitude of $y(s)$, the time derivatives $\dot{y}$ and $\dot{S}$ are related by

$$\dot{y}(s) = \tfrac{1}{2}(\dot{S}/S) y(s) \tag{13}$$

Using the static buckling profile, Eq. 5, for $y(s)$ (i.e., to linear order in the kinetics), the instantaneous viscous dissipation W due to the lateral motion is then found to be

$$W = c_\perp \int_0^L ds (\dot{y})^2 = \frac{5}{6} \frac{c_\perp L^2}{\gamma^2} (\dot{S}^2/S) \tag{14}$$

where $c_\parallel$ is the lateral drag coefficient per unit length for the microtubule (see Hunt et al., 1994). We can also express the initial dissipation using the motor force $F_\parallel$ and the buckling force F_B as $W = (F_\parallel - F_B)\dot{S}$; combining this with Eqs. 13 and 14 gives

$$\frac{\dot{y}}{y} = \frac{\gamma^2}{c_\perp L^2} (F_\parallel - F_B) \tag{15}$$

showing that, for an excess force $F_\parallel - F_B$, $y(s, t)$ rises exponentially,

$$y(s, t) = y(s, 0) \exp\left[\frac{3}{5} \frac{\gamma^2}{c_\perp L^2} (F_\parallel - F_B) t\right] \equiv y(s, 0) \exp(t/T). \tag{16}$$

(defining T). Here $y(s,0)$ may be regarded as an initial deviation (intrinsic or thermal) from straightness; the filament will soon assume the shape of the linear buckling profile as it grows under the compressive force.

The value of $c_\parallel$ estimated for microtubules in a motility assay is $11.9 \pm 1.1 \times 10^{-3}$ N·s·m^{-2} (Hunt et al., 1994). In Eq. 16 this gives a rise time of $T \approx (1.0 \text{ ms·pN/}\mu\text{m}^2) \times L^2/(F_\parallel - F_B)$, which is proportional to the square of the buckling length, and inversely proportional to the excess motor force over the critical buckling force. A 10-μm microtubule under a motor load 1 pN over the buckling force should have a rise time of $T = 100$ ms. Viscous kinetics might be observable in the buckling of long microtubules, or for forces very near the critical buckling force. However, they should not dominate the force estimates found in this paper.

In Fig. 6 *c*, we show an example of displacement versus time (obtained as in Fig. 6 *a*) for the longest buckling-length microtubule that was digitized ($L_B = 12.2$ μm). T should be relatively large in this event. In this case, however, as well as in two other cases ($L_B = 11.8$ μm and $L_B = 11.4$ μm, not shown) the onset of motion was clear and abrupt, confirming that even in these cases, no hydrodynamic slowing is apparent.

APPENDIX C: APPLICABILITY OF ELASTIC BENDING THEORY

The bending theory that has been used here assumes no longitudinal compression of the filament. Compression is in fact negligible because of the Euler buckling instability itself (Eq. 1) as follows. The maximum compressive force $F_\parallel$ of a filament of length L can only be attained if the filament is straight, in which case by the definition of the Young's modulus E (Landau and Lifshitz, 1986) the longitudinal compression is

$$\Delta x = F_\parallel L/EA. \tag{17}$$

The cross-sectional area A of the microtubule (with inner radius r_i and outer radius r_o) is $A = \pi(r_o^2 - r_i^2)$. To be stable against buckling, the Euler condition is $F_\parallel \le F_B = EI\,\gamma^2/L^2$ (where $\gamma = 4.493$). Finally, $I = \pi(r_o^4 - r_i^4)/4$ for a hollow cylinder (Gittes et al., 1993). Using these relations in Eq. 17 gives

$$\Delta x \le \frac{F_B L}{EA} = \frac{\gamma^2}{4L} (r_o^2 + r_i^2). \tag{18}$$

Using $r_o^2 + r_i^2 \approx (20 \text{ nm})^2$ for microtubules, and $L \approx 10$ μm, the longitudinal compression is $\Delta x \approx 4$ Å over the entire length of the filament, which is negligibly small.

We also ask what quantitative degree of bending might be expected to result in nonlinear elastic behavior, or even damage to the tubulin polymer,

that would cause linear elastic bending theories to fail. By starting with a quadratic bending free energy $g(s)$ (see Appendix A), we assumed that linear elasticity applies to the bending microtubules (not to be confused with linearized bending equations such as Eq. 6). If a microtubule is bent with a radius of curvature R, the compression and extension of the microtubule on the inside and outside of the bend, per tubulin monomer of length a, is

$$\Delta s = \pm a\Delta r/R \tag{19}$$

If one asks for a maximum distortion of $\Delta s = \pm 1$ Å in the 40 Å monomers, for example, this corresponds to $R = 0.5$ μm, a very small radius of curvature. It seems safe to assume that linear elasticity does apply.

APPENDIX D: BUCKLING LENGTH STATISTICS

$f_0(L_B)$ is the probability per unit length that a kinesin motor a distance L_B from the clamped section of a microtubule will buckle it. But f_0 must be multiplied by two factors that depend on the length L_+ of the plus-end region of the microtubule (see Fig. 1 *a*):

i) First we must include the probability $P_1(L_+)$ that exactly one motor is able to interact with the microtubule, because events were rejected when more than one motor was involved in the onset of buckling (Materials and Methods). If a density ρ of kinesin motors is attached to the surface, and each motor can reach a distance a from its point of attachment, then $2a\rho$ motors per unit length interact with the microtubule. Using Poisson statistics,

$$P_1(L_+) = e^{-2a\rho L_+}. \tag{20}$$

ii) Second, we must multiply by the population $n(L_+)$ of clamped microtubules with $L_+ > L_B$ that are competent to buckle. At this point we make an assumption, to be confirmed below, that

$$n(L_+)P_1(L_+) \equiv (\text{const.}) \times e^{-\alpha L_+}, \tag{21}$$

i.e., either $n(L_+)$ decreases much more slowly than $P_1(L_+)$ (in which case $\alpha \cong 2a\rho$, using Eq. 21), or else $n(L_+)$ resembles a decreasing exponential over the observed L_+ (in which case $\alpha > 2a\rho$).

The experimental distribution of buckling events $f_{exp}(L_+, L_B)$ is the product of $f_0(L_B)$ with Eq. 21, plus the requirement that $L_B < L_+$:

$$f_{exp}(L_+, L_B) = \begin{cases} (\text{const.}) \times f_0(L_B)e^{-\alpha L_+}, & L_B \le L_+ \\ 0, & L_B > L_+ \end{cases}. \tag{22}$$

Fitting Eq. 22 to data is difficult because L_B and L_+ are not statistically independent for all data points (because of the $L_B < L_+$ cutoff). However, L_B and $L_+ - L_B$ are independent;

$$f_{exp}(L_+, L_B) = (\text{const.}) \times f_0(L_B)e^{-\alpha L_B} \times e^{-\alpha(L_+ - L_B)} \tag{23}$$

holds for all data points, and $L_+ - L_B$ is distributed exponentially with decay constant α.

Experimental buckling data are shown in Fig. 11 as a scatter plot in L_+ and L_B. A small gap between the data and the $L_+ = L_B$ line shows that $L_+ - L_B$ is overestimated by about 0.5 μm because of a resolution error in estimating L_+ or L_B or both. Fig. 11 (*inset*) shows that a histogram of $L_+ - L_B$ indeed decays exponentially with $\alpha^{-1} = 2.80 \pm 0.22$ μm (including 0.5 μm as just mentioned), confirming our assumption of Eq. 21.

The parameter α is all that is needed to recover the unbiased event distribution $f_0(L_B)$. The L_B histogram $H(L_B)$, in Fig. 3 *a*, is related to

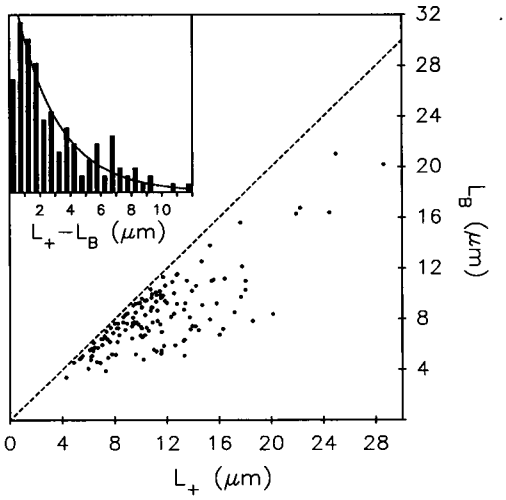

FIGURE 11 Plot of microtubule buckling length L_B, versus length L_+ of the unclamped plus end, for the 142 buckling events of Fig. 3 *a* (see also Fig. 1 *a* for definitions of L_B and L_+). The form of a joint distribution for L_B and L_+ allows an estimate of two biases present in Fig. 3. A small gap between the data and the $L_+ = L_B$ line are due to error in resolving segment ends. (*Inset*) Histogram of the difference $L_+ - L_B$ for all events, with a fitted exponential. The exponential decay length α^{-1} of this particular quantity can be used to compensate for biases in the buckling-length histograms of Fig. 3.

$f_0(L_B)$ by

$$H(L_B) = \int_0^\infty f_{exp}(L_+, L_B)\, dL_+ = (\text{const.}) \times f_0(L_B)e^{-\alpha L_B}. \tag{24}$$

With $\alpha^{-1} = 2.80 \pm .22$ μm,

$$f_0(L_B) = (\text{const.}) \times H(L_B) \times \exp(L_B/2.80\ \mu\text{m}). \tag{25}$$

Using $H(L_B)$ from Fig. 3 *a*, the resultant $f_0(L_B)$ was shown in Fig. 4, up to a constant factor.

F. G. would like to acknowledge valuable discussions with Albert Gordon, Brian Mickey, Dave Coy, Will Hancock, Pedro Verdugo, and Tom Daniel, who suggested the relevance of drag effects. Charles Brokaw provided helpful comments on the manuscript.

F. G. was supported in part by a Mathematical Biology fellowship from the National Science Foundation (BIR 9256532) and by the National Institutes of Health (AR40593). J. H. was a Pew Scholar in the Biomedical Sciences. E. M. was supported by a fellowship from the American Heart Association, Washington affiliate. This work was supported by the Human Frontier Science Program.

REFERENCES

Allen, R. D., D. G. Weiss, J. H. Hayden, D. T. Brown, H. Fujiwake, and M. Simpson. 1985. Gliding movement of and bidirectional movement along single native microtubules from squid axoplasm: evidence for an active role of microtubules in cytoplasmic transport. *J. Cell Biol.* 100: 1736–1752.

Amos, L. A., and W. B. Amos. 1991. The bending of sliding microtubules imaged by confocal light microscopy and negative stain electron microscopy. *J. Cell Sci. Suppl.* 14:95–101.

Block, S. M., L. S. B. Goldstein, and B. J. Schnapp. 1990. Bead movement by single kinesin molecules studied with optical tweezers. *Nature.* 348:348–352.

Bourdieu, L., T. Duke, M. B. Elowitz, D. A. Winkelmann, S. Leibler, and A. Libchaber. 1995. Spiral defects in motility assays: a measure of motor protein force. *Phys. Rev. Lett.* 75:176–179.

Brady, S. T. 1985. A novel brain ATPase with properties expected for the fast axonal transport motor. *Nature.* 317:73–75.

Brokaw, C. J. 1975. Cross-bridge behavior in a sliding filament model for flagella. *In* Molecules and Cell Movement. S. Inoué and R. E. Stephens, editors. Raven Press, New York. 165–179.

Chrétien, D., F. Metoz, F. Verde, E. Karsenti, and R. H. Wade. 1992. Lattice defects in microtubules: protofilament numbers vary within individual microtubules. *J. Cell Biol.* 117:1031–1040.

De Donder, T., and P. van Rysselberghe. 1936. The Thermodynamic Theory of Affinity. Stanford University Press, Stanford, CA.

de Groot, S. R., and P. Mazur. 1962. Non-Equilibrium Thermodynamics. North-Holland, Amsterdam.

Gittes, F., B. Mickey, J. Nettleton, and J. Howard. 1993. Flexural rigidity of microtubules and actin filaments measured from thermal fluctuations in shape. *J. Cell Biol.* 120:923–934.

Gradshteyn, I. S., and I. M. Ryzhik. 1980. Table of Integrals, Series, and Products, 4th Ed. Academic Press, London.

Hill, T. L. 1974. Theoretical formulation for the sliding-filament model of contraction of striated muscle. *Prog. Biophys. Mol. Biol.* 28:267–340.

Howard, J., A. J. Hudspeth, and R. D. Vale. 1989. Movements of microtubules by single kinesin molecules. *Nature.* 342:154–158.

Howard, J., A. J. Hunt, and S. Baek. 1993. Assay of microtubule movement driven by single kinesin molecules. *Methods Cell Biol.* 39:137–147.

Howard, J., and A. A. Hyman. 1993. Preparation of marked microtubules for the assay of the polarity of microtubule-based motors by fluorescence microscopy. *Methods Cell Biol.* 39:105–113.

Hunt, A. J., F. Gittes, and J. Howard. 1994. The force exerted by kinesin against a viscous load. *Biophys. J.* 67:766–781.

Hunt, A. J., and J. Howard. 1993. Kinesin swivels to permit microtubule movement in any direction. *Proc. Natl. Acad. Sci. USA.* 90:11653–11657.

Huxley, A. F. 1957. Muscle structure and theories of contraction. *Prog. Biophys. Biophys. Chem.* 7:255–318.

Hyman, A., D. Drechsel, D. Kellogg, S. Salser, K. Sawin, P. Steffen, L. Wordeman, and T. Mitchison. 1991. Preparation of modified tubulins. *Methods Enzymol.* 196:478–485.

Landau, L. D., and E. M. Lifshitz. 1986. Theory of Elasticity, 3rd Ed. Pergamon Press, Oxford.

Leibler, S., and D. A. Huse. 1993. Porters versus rowers: a unified stochastic model of motor proteins. *J. Cell Biol.* 121:1357–1368.

Love, A. E. H. 1927. A Treatise on the Mathematical Theory of Elasticity, 4th Ed. Cambridge University Press, New York.

Meyhöfer, E., and J. Howard. 1995. The force generated by a single kinesin molecule against an elastic load. *Proc. Natl. Acad. Sci. USA.* 92:574–578.

Peskin, C. S., and G. Oster. 1995. Coordinated hydrolysis explains the mechanical behavior of kinesin. *Biophys. J.* 68:202s–211s.

Press, W. H., S. A. Teukolsky, W. T. Vetterling, and B. P. Flannery. 1992. Numerical Recipes in C, 2nd Ed. Cambridge University Press, New York.

Ray, S., E. Meyhöfer, R. A. Milligan, and J. Howard. 1993. Kinesin follows the microtubule's protofilament axis. *J. Cell Biol.* 121: 1083–1093.

Svoboda, K., and S. M. Block. 1994. Force and velocity measured for single kinesin molecules. *Cell.* 77:773–784.

Vale, R. D., T. S. Reese, and M. P. Sheetz. 1985. Identification of a novel force-generating protein, kinesin, involved in microtubule-based motility. *Cell.* 42:39–50.

Wagner, M. C., K. K. Pfister, S. T. Brady, and G. S. Bloom. 1991. Purification of kinesin from bovine brain and assay of microtubule-stimulated ATPase activity. *Methods Enzymol.* 196:157–175.

Weingarten, M. D., M. M. Suter, D. R. Littman, and M. W. Kirschner. 1974. Properties of the depolymerization products of microtubules from mammalian brain. *Biochemistry.* 13:5529–5537.